

Mean field and beyond-mean-field global calculations with Gogny interactions

Tomás R. Rodríguez,^{1,2} Alexander Arzhanov,² and Gabriel Martínez-Pinedo^{2,3}

¹*Departamento de Física Teórica, Universidad Autónoma de Madrid, E-28049 Madrid, Spain*

²*Institut für Kernphysik, Technische Universität Darmstadt, D-64289 Darmstadt, Germany*

³*GSI Helmholtzzentrum für Schwerionenforschung, Planckstraße 1, 64291 Darmstadt, Germany*

(Dated: June 4, 2022)

Self-consistent mean field (MF) and beyond-mean-field (BMF) calculations of masses, separation energies and 2_1^+ excitation energies of even-even nuclei where experimental data is available are presented. The functionals used are based on the Gogny D1S and D1M parametrizations and the method includes beyond-mean-field corrections coming from both exact shape mixing and exact symmetry restorations without assuming gaussian overlap approximations. A comparison between mean field, beyond-mean-field approaches and the experimental data is provided.

PACS numbers: 21.10.Dr, 21.60.Jz, 21.60.Ev, 21.30.-x

I. INTRODUCTION

Nuclear binding energies are one of the most relevant quantities that define the atomic nucleus. Apart from their intrinsic interest, the nuclear masses are specially important in determining the nucleosynthesis processes that occur in astrophysical environments. For example, they determine the limits of existence of the nucleus as a bound system of protons and neutrons (drip lines), the Q -values for β and α decays, the particle separation energies that are needed to compute capture/emission rates, etc. Therefore, a great effort in measuring masses of very exotic (short-lived) nuclei with high precision is currently made with the use of trapping and/or storage rings techniques [1].

Despite this significant progress, and the one expected in the near future with the arrival of new facilities worldwide, many nuclei will not be experimentally reachable. Particularly important are those belonging to neutron rich regions that are relevant to better constraint the rapid neutron capture (r-process) nucleosynthesis, the mechanism behind the origin of more than the half of the elements beyond iron in the universe. Hence, nuclear models able to compute with high precision the known masses, as well as to provide reliable extrapolations, are very much demanded.

Current theoretical nuclear mass tables are provided mainly by three different approaches: (a) Microscopic-macroscopic (mic-mac) methods which improve the original liquid drop formula with microscopic corrections. The most commonly used of this kind are the finite range droplet model (FRDM) [2] or, more recently, the Weizsäcker-Skyrme (WS) mass model [3]. (b) Duflo-Zuker (DZ) approach based a functional of occupation numbers guided by the interacting shell model method [4]. (c) Microscopic methods based on Hartree-Fock-Bogoliubov (HFB) approaches with Skyrme (see Ref. [5] and references therein) and Gogny functionals [6]. All of the above methods have reached a root mean square (RMS) deviation from the most recent data between around 0.5 MeV.

This impressive agreement to the global behavior of the known masses is not sufficient to have a full confidence in the extrapolations to unknown regions since large deviations in the predictions of the different models are found. In addition, even if the overall performance is similar, some local deviations between the models in sensitive regions can largely affect the results of nucleosynthesis simulations [7, 8]. Therefore, theoretical models should be improved to reduce such uncertainties. In particular, *ab-initio* calculations are becoming available for medium mass systems although currently neither the range of applicability nor the accuracy reached by such methods are good enough to be applied to astrophysical purposes [9–13]. Hence, in the short-mid term effective energy density functionals are still the most promising microscopic methods to compute nuclear properties in the whole nuclear chart with the required accuracy. These methods have been improved significantly in the last years by taking into account not only global fits to all known masses but also some constraints coming from *ab-initio* calculations in infinite nuclear matter [5, 14, 15].

However, a mean field (HFB) approach is commonly used to solve the nuclear many-body problem and beyond-mean-field (BMF) corrections have been included phenomenologically to mimic rotational and vibrational corrections [16]. Nevertheless, in the last decade, a better treatment of such BMF correlations of even-even nuclei using symmetry restorations and configuration mixing methods have been implemented with Skyrme, Relativistic and Gogny interactions [17]. These improvements have allowed the study of the appearance/disappearance of shell closures or shape mixing/coexistence/transitions phenomena, for example. Concerning nuclear masses, these BMF correlations have been computed globally using particle number and angular momentum projection and generator coordinate method (GCM) with Skyrme interactions [18, 19] and using the five dimensional collective hamiltonian (5DCH) with Gogny interactions [6, 20]. Due to the large computational burden of performing exact GCM with exact particle number and angular momentum restorations, these pioneer global surveys were carried out assuming gaussian overlap approximations.

In this paper we present the results of global calculations for even-even nuclei performed with the Gogny D1S [21, 22] and D1M [6] interactions using exact implementations of the GCM and quantum number projection methods. This document is organized as follows: First, a description of the method used to compute masses is given in Sec. II. Then, the results are discussed in Sec. III. Finally, a brief summary and outlook are presented in Sec. IV.

II. THEORETICAL FRAMEWORK

The total energy (negative in our convention) of a given nucleus is calculated in the present work as the sum of two terms:

$$E = E_{\text{HFB}} + \Delta E_{\text{BMF}} \quad (1)$$

where E_{HFB} is the Hartree-Fock-Bogoliubov (HFB) energy (mean field) and ΔE_{BMF} is a beyond-mean-field (BMF) correction which includes particle number restoration, angular momentum projection and axial quadrupole shape mixing within the generator coordinate method (GCM) [23]. Both terms are computed with the same underlying interaction, namely, Gogny D1S or D1M parametrization.

For the sake of simplifying the notation, we express the theoretical energy throughout this work as the expectation value of a hamiltonian operator. However, it is important to point out that since the effective interactions used here are density-dependent, this notation is not truly rigorous and energy density functionals (EDFs) should be defined instead of such expectation values. We refer to Ref. [24] for a general discussion about this topic and Refs. [25, 26] for the particular choice of the corresponding EDFs used in this work.

A. Mean field (HFB) approach

We start by reviewing briefly the HFB method [23]. In this microscopic approach, based on the variational principle, the many-body wave function of the atomic nucleus is considered to be a quasiparticle vacuum, $|\text{HFB}\rangle$:

$$\hat{\beta}_k |\text{HFB}\rangle = 0 \quad \forall k \quad (2)$$

Those quasiparticles are defined as the most general linear combination of creation (\hat{c}_l^\dagger) and annihilation (\hat{c}_l) single particle operators:

$$\hat{\beta}_k^\dagger = \sum_l U_{lk} \hat{c}_l^\dagger + V_{lk} \hat{c}_l, \quad (3)$$

where U , and V are the variational parameters. Since Eq. 3 breaks most of the symmetries of the original interaction, in particular, the particle number symmetry,

the HFB wave function is constrained to have the correct mean value of the number of particles. Therefore, the HFB equations [23] are found by the condition:

$$\delta \left(E'_{\text{HFB}} [|\phi\rangle] \right)_{|\phi\rangle=|\text{HFB}\rangle} = 0 \quad (4)$$

with

$$E'_{\text{HFB}} [|\phi\rangle] = \langle \phi | \hat{H} | \phi \rangle - \lambda_N \langle \phi | \hat{N} | \phi \rangle - \lambda_Z \langle \phi | \hat{Z} | \phi \rangle, \quad (5)$$

where \hat{H} , \hat{N} (\hat{Z}) are the hamiltonian and the neutron (proton) number operators, respectively; $|\phi\rangle$ are HFB-like states, i.e., they fulfill the condition given in Eq. 2; and $\lambda_{N(Z)}$ is a Lagrange multiplier which ensures $\langle \phi | \hat{N} (\hat{Z}) | \phi \rangle = N (Z)$. The normalization $\langle \phi | \phi \rangle = 1$ is also assumed. By solving the corresponding HFB equations, the matrices U, V of the transformation given in Eq. 3 define the state $|\text{HFB}\rangle$ from which the HFB energy is computed.

In practical applications, the spherical harmonic oscillator (s.h.o.) basis is usually chosen as the working basis where the quasiparticles defined in Eq. 3 are expanded. The sum in such an equation runs over an infinite number of s.h.o. states but this sum must be truncated in actual implementations in computer codes. The results should not depend on the choice of the basis and the convergence of the results are obtained if a sufficiently large number of major s.h.o. shells ($N_{s.h.o.}$) are included. However, the computational burden increases significantly with the number of oscillator shells and a compromise between a better convergence and a reasonable computational time has to be considered. In the present work, E_{HFB} in Eq. 1 is computed with $N_{s.h.o.} = 19$.

B. Beyond-mean-field (BMF) approach

The second term in the energy (ΔE_{BMF} in Eq. 1) corresponds to corrections beyond the mean field (HFB) approximation. In principle, the energy should be computed by using BMF methods from the first place. However, these methods are much more time consuming than the corresponding HFB and the size of the s.h.o. basis used in this case is generally smaller. In the present manuscript, $N_{s.h.o.} = 11$ has been chosen for computing BMF effects. Hence, BMF correction is defined as:

$$\Delta E_{\text{BMF}} = E_{\text{BMF}}(N_{s.h.o.} = 11) - E_{\text{HFB}}(N_{s.h.o.} = 11) \quad (6)$$

where in this expression we assume that the BMF corrections converge with the size of the working basis faster than the total energies. We will give an explicit example in Sec. III A.

In the above equation, $E_{\text{BMF}}(N_{s.h.o.} = 11)$ is computed within a symmetry conserving configuration mixing (SCCM) framework. This method is variationally consistent with the underlying mean field, i.e., lower total energies are always obtained when such correlations

are taken into account. The method contains simultaneous particle number and angular momentum projection (PNAMP) of different intrinsic Hartree-Fock-Bogoliubov type states (HFB) and a subsequent mixing of these states performed within the generator coordinate method (GCM) framework. In general, different shapes (axial and non-axial) and collective coordinates can be included in the GCM calculation. However, the addition of more generating coordinates largely increases the computational time, especially if a triaxial angular momentum projection is performed. Therefore, we have focused on the mixing of axial deformed states. Further extensions will be explored in a future study. In the following, the particular realization of the SCCM method used here is described step-by-step.

1. Variation after particle number projection method (PN-VAP)

In contrast to the previous section, the HFB-type states ($|\text{PNVAP}(\beta_2)\rangle$), are found through a variation after particle number projection method (PN-VAP) with constraints in the axial quadrupole deformation degree of freedom (β_2) [23, 28]. Hence, the particle number projected energy is minimized instead of the HFB one. Furthermore, shape mixing in the final state is allowed by exploring the quadrupole deformation explicitly. The variational equation now reads as:

$$\delta \left(E'_{\text{PN-VAP}} [|\phi\rangle] \right)_{|\phi\rangle=|\text{PNVAP}\rangle} = 0, \quad (7)$$

with

$$E'_{\text{PN-VAP}} [|\phi\rangle] = \frac{\langle \phi | \hat{H} P^N P^Z | \phi \rangle}{\langle \phi | P^N P^Z | \phi \rangle} - \lambda_{q_{20}} \langle \phi | \hat{Q}_{20} | \phi \rangle. \quad (8)$$

$P^{N(Z)}$ is the projector onto good number of neutrons (protons) [23]. $\hat{Q}_{20} = r^2 Y_{20}(\theta, \varphi)$ is the axial quadrupole operator and the Lagrange multiplier $\lambda_{q_{20}}$ ensures the condition: $\lambda_{q_{20}} \rightarrow \langle \phi | \hat{Q}_{20} | \phi \rangle = q_{20}$. The quadrupole deformation parameter β_2 is related to q_{20} by:

$$q_{20} = \pm \frac{\beta_2}{C}; \quad C = \sqrt{\frac{5}{4\pi}} \frac{4\pi}{3r_0^2 A^{5/3}} \quad (9)$$

being $r_0 = 1.2$ fm, A the mass number and the plus (minus) sign indicates prolate (oblate) shapes. Hence, the collective intrinsic deformation is well established within this framework and this fact allows the description of the states in the laboratory frame in terms of their intrinsic shapes unambiguously.

2. Symmetry conserving configuration mixing (SCCM) method

Once the set of wave functions $|\text{PNVAP}(\beta_2)\rangle$ is obtained, the final states are built through the Ansatz provided by the generator coordinate method (GCM) [23]. In this framework, the states are assumed to be linear combinations of particle number and angular momentum projected PN-VAP states:

$$|\Psi^{I\sigma}\rangle = \sum_{\beta_2} g_{\beta_2}^{I\sigma} P_0^I P^N P^Z |\text{PNVAP}(\beta_2)\rangle \quad (10)$$

where I is the total angular momentum, $P_{KK'}^I$ the angular momentum projector applied to axial symmetric intrinsic states ($K = K' = 0$) [23] and σ labels different states obtained for a given value of I . The parameters $g_{\beta_2}^{I\sigma}$ are determined by the Ritz variational principle which leads to the Hill-Wheeler-Griffin (HWG) equation:

$$\delta (E_{\text{SCCM}}^{I\sigma} [g_{\beta_2}^{I\sigma}]) = 0 \Rightarrow \sum_{\beta'_2} \left(\mathcal{H}_{\beta_2, \beta'_2}^I - E_{\text{SCCM}}^{I\sigma} \mathcal{N}_{\beta_2, \beta'_2}^I \right) g_{\beta'_2}^{I\sigma} = 0 \quad (11)$$

The energy and norm overlap matrices are defined as:

$$\begin{aligned} \mathcal{H}_{\beta_2, \beta'_2}^I &= \langle \text{PNVAP}(\beta_2) | \hat{H} P_0^I P^N P^Z | \text{PNVAP}(\beta'_2) \rangle \\ \mathcal{N}_{\beta_2, \beta'_2}^I &= \langle \text{PNVAP}(\beta_2) | P_0^I P^N P^Z | \text{PNVAP}(\beta'_2) \rangle \end{aligned} \quad (12)$$

The resulting HWG equations -one for each value of the angular momentum- provide the energy levels $E_{\text{SCCM}}^{I\sigma}$ and collective wave functions defined in the (β_2) direction.

Hence, the energy including symmetry restorations and shape mixing within this framework is given by:

$$E_{\text{BMF}}(N_{s.h.o.} = 11) = E_{\text{SCCM}}^{I=0\sigma=1} \quad (13)$$

Obviously, excited states, in particular $E(2_1^+) = E_{\text{SCCM}}^{I=2\sigma=1} - E_{\text{SCCM}}^{I=0\sigma=1}$ excitation energies, can be also calculated within the same framework.

We summarize some details about the actual calculations. First of all, the HFB [32], PN-VAP [28] and SCCM [27] codes used throughout this work have been developed in the Nuclear Physics Group at the Universidad Aut3noma de Madrid. The calculations were performed both in GSI-Prometheus (Darmstadt) [33] and CSC-Loewe (Frankfurt) [34] computing facilities, using scripts optimized to perform such a large scale survey. The HFB (mean field) solutions have been found by using a spherical harmonic oscillator basis with $N_{s.h.o.} = 19$ shells and an optimized oscillator length for each nu-

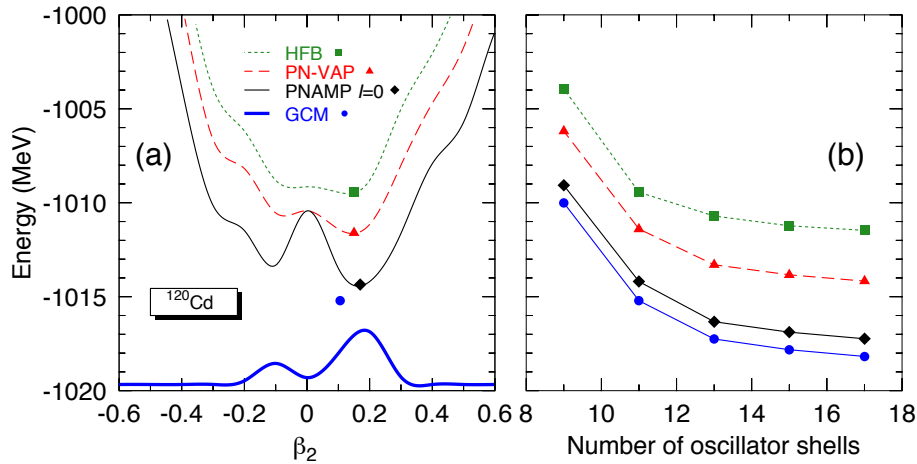


FIG. 1. (a) Potential energy surfaces as a function of the axial quadrupole deformation calculated with HFB (green dotted line), PN-VAP (red dashed line) and PNAMP (thin black continuous line) approximations for ^{120}Cd with the Gogny D1S parametrization. The square, triangle and diamond represent the minima of each surface respectively. The blue dot corresponds to the full SCCM energy and the blue thick continuous line is the ground state collective wave function. The arrows point out the energy gain between the different approaches considered in this work. (b) Convergence of the energy as a function of the number of major oscillator shells included in the working basis for the same approaches of the left panel.

cleus [31]. Additionally, potential energy surfaces along the axial quadrupole degree of freedom were explored to make sure that the unconstrained HFB-calculations did not converge to local meta-stable minima. All terms (direct, exchange and pairing) in the interaction (including Coulomb) have been included here and also in the BMF part. In this case, a set of 15-20 intrinsic many-body wave functions with different axial quadrupole shapes (oblate and prolate) has been found by using the PN-VAP method described above. These intrinsic wave functions are expanded in a basis with $N_{s.h.o.} = 11$ shells, again with an optimized oscillator length for each nucleus. The standard number of points used in the integrals in the gauge (particle number projection) and Euler (angular momentum projection) angles were 9 and 16 respectively and the convergence of the quantum number projections were checked by inspecting the mean values of the operators, \hat{N} , \hat{Z} , $\Delta\hat{N}^2$, $\Delta\hat{Z}^2$ and \hat{J}^2 .

Finally, the convergence of the solutions of the HWG equations has been ensured by analyzing the energy plateaus as a function of the natural states which transform the HWG equations into regular eigenvalue problems. Detailed expressions and performance of this approach can be found in Refs. [26, 27] (and references therein).

III. RESULTS

A. BMF correlation energies

To shed light on how the BMF method used here actually works, the nucleus ^{120}Cd is taken as an example. The

HFB -Gogny D1S- energy calculated with $N_{s.h.o.} = 19$ is $E_{\text{HFB}} = -1011.786$ MeV. On top of this value, BMF corrections are made (see Eq. 1). As it is mentioned in the previous section, these corrections are performed with $N_{s.h.o.} = 11$. In Fig. 1 the energy as a function of the axial quadrupole deformation β_2 is represented for mean field (HFB, dotted line), variation after particle number projection (PN-VAP, dashed line) and particle number and angular momentum $I = 0$ projection (PNAMP, $I = 0$, thin continuous line) approximations. The minima of each potential energy surfaces are the corresponding energies for each level of approximation (square, HFB; triangle PN-VAP; and diamond PNAMP, $I = 0$). In this case, the value of deformation of all the minima is quite similar ($\beta_2 \approx 0.17$), i.e., ^{120}Cd is prolate deformed in all of these approaches. A gain in the energy (1.96 MeV) is observed when correlations associated to the restoration of the particle number are taken into account. Further correlation energy (2.80 MeV) is obtained when simultaneous particle number and angular momentum projection is performed. In addition, by allowing shape mixing of particle number and angular momentum restored axial states (GCM), Eqs. 10-11, the energy marked by a blue dot in Fig. 1 is obtained, i.e., 1.02 MeV extra energy with respect to the PNAMP ($I = 0$) minimum. In continuous thick blue line, the so-called ground state collective wave function is plotted and it represents the probability of having a given β_2 deformation in this state. In this case, two maxima are found at $\beta_2 \approx -0.1$ and $+0.2$, being the prolate one the absolute maximum. The position of the blue dot in the abscissa axis corresponds to the mean deformation calculated with the ground state collective wave function $\beta_2 = 0.10$. In summary, the

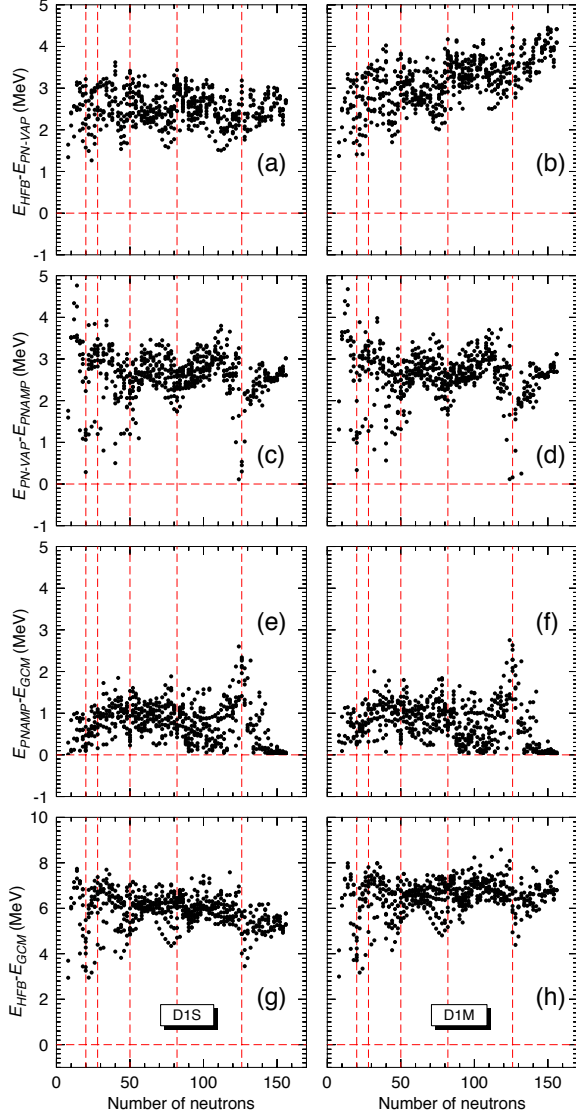


FIG. 2. (color online) Gain in total energy as a function of the number of neutrons obtained by including (a)-(b) variation after particle number projection (PN-VAP) method; (c)-(d) Simultaneous particle number and angular momentum $I = 0$ projection (PNAMP); (e)-(f) quadrupole shape mixing within the generator coordinate method (GCM) with symmetry restored states; and (g)-(h) total beyond-mean-field gain. Dashed vertical lines represent the neutron magic numbers 20, 28, 50, 82 and 126. Left and right panels correspond to Gogny D1S and D1M parametrizations, respectively.

total correction provided by the current SCCM method is $\Delta E_{\text{BMF}} = 5.77$ MeV and the total energy (Eq. 1) is $E(^{120}\text{Cd}) = -1017.559$ MeV.

We now generalize these results to the even-even nuclei with $Z, N \geq 10$ contained in the most recent Atomic Mass Evaluation (AME) [29] both for Gogny D1S and D1M parametrizations. In Fig. 2 the successive gains in total energy reached by restoring the symmetries and

allowing the axial quadrupole shape mixing are represented as a function of the number of neutrons. For the D1S parametrization we observe a band of values ranged in the interval 1.5–3.5 MeV with a mean gain ~ 2.3 MeV of correlation energy with respect to the mean field (HFB) solutions when variation after particle number projection (PN-VAP) method is applied (Fig 2(a)). Within the same approach (PN-VAP), we obtain a drift towards larger energy gains when increasing the number of neutrons in the D1M results (Fig. 2(b)), reaching up to ~ 4.5 MeV gain for heavy nuclei in this case. In addition, some local minima are obtained around $\sim 24, \sim 44, \sim 78$ and ~ 110 , right before the neutron magic numbers 28, 50, 82 and 126 for both D1S and D1M parametrizations.

Minima are found both in the energy gained by particle number and angular momentum restoration (PNAMP) -on top of PN-VAP- and by the generator coordinate method (GCM) -on top of PNAMP at shell closures. In the former (Figs. 2(c)-(d)), larger correlation energies are obtained in the mid-shell and minima are found at the neutron magic numbers. Excluding the lighter and the semi-magic nuclei, an average gain of ~ 2.7 MeV is attained and a slightly decreasing slope is also observed when increasing the number of neutrons. Concerning the GCM correlation energies (Figs. 2(e)-(f)), contrary to PNAMP, the larger gains are almost at the shell closures, obtaining a clear maximum at $N = 126$. The average gain in this case is ~ 0.8 MeV. It is important to point out that the behavior of PNAMP and GCM correlation energies are strikingly similar for D1S and D1M parametrizations. This behavior of the BMF energies is important to correct the parabolic shape observed in experimental theoretical energy differences at the HFB level (see fig. 5).

Finally, the total beyond-mean-field energy gain (summing up all of the previous contributions) is represented in Figs. 2(g)-(h). We observe first that smaller correlation energies are obtained around the magic numbers, producing qualitatively an inverted parabolic behavior between two consecutive shell closures. Furthermore, we see a larger spread in the BMF energy gain in the lighter nuclei. Finally, the overall gain is rather flat for the D1M results, while for the D1S parametrization a slightly smaller average gain is obtained when the number of neutrons is increased.

Analogous patterns as the ones just described above are found for the different levels of approximation when they are represented as a function of the number of protons (see Fig. 3). Hence, a positive slope in the energy gain for the PN-VAP approach is obtained for D1M parametrization while for D1S the net gain is flatter. Furthermore, the local minima are found now at the proton magic numbers 20, 28, 50 and 82 in this approximation. For PNAMP and GCM approaches we do not observe differences between the parametrizations. In the former, shell effects are still present at $Z = 20, 28, 40$ and 82; in the latter, the lead isotopes have the most prominent

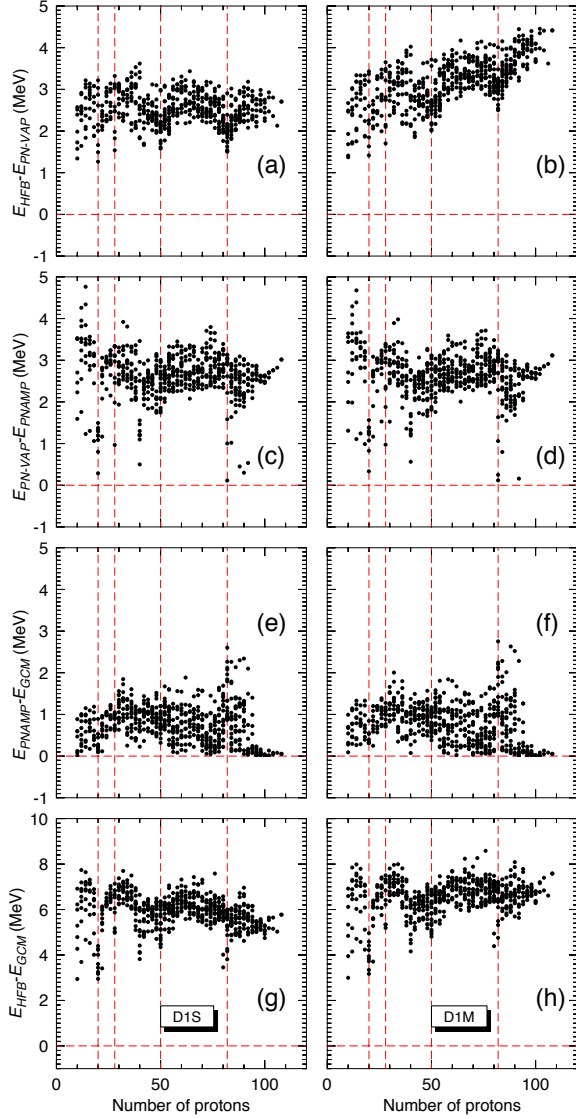


FIG. 3. Same as Fig. 2 but as a function of the number of protons. Dashed vertical lines represent the proton magic numbers 20, 28, 50 and 82.

ones.

Since both PNAMP and GCM methods depend crucially on the intrinsic deformation, we also represent the correlation energy gains obtained for the different approaches as a function of the quadrupole deformation β_2 obtained at the HFB level for each nucleus (Fig. 4). In all cases, the largest spread in correlation energy gain is obtained in the spherical point $\beta_2 = 0$. Hence, for this intrinsic deformation we observe with the D1S (D1M) parametrization energy gains ranging from 1.2-3.5 (1.5-4.5) MeV, 0.0-3.7 (0.0-3.5) MeV and 0.0-2.7 (0.0-2.8) MeV for PN-VAP, PNAMP, and GCM, respectively. These spreads are smaller for the rest of deformations. Additionally, the energy gain does not depend very much on the size and sign of the quadrupole deformation both

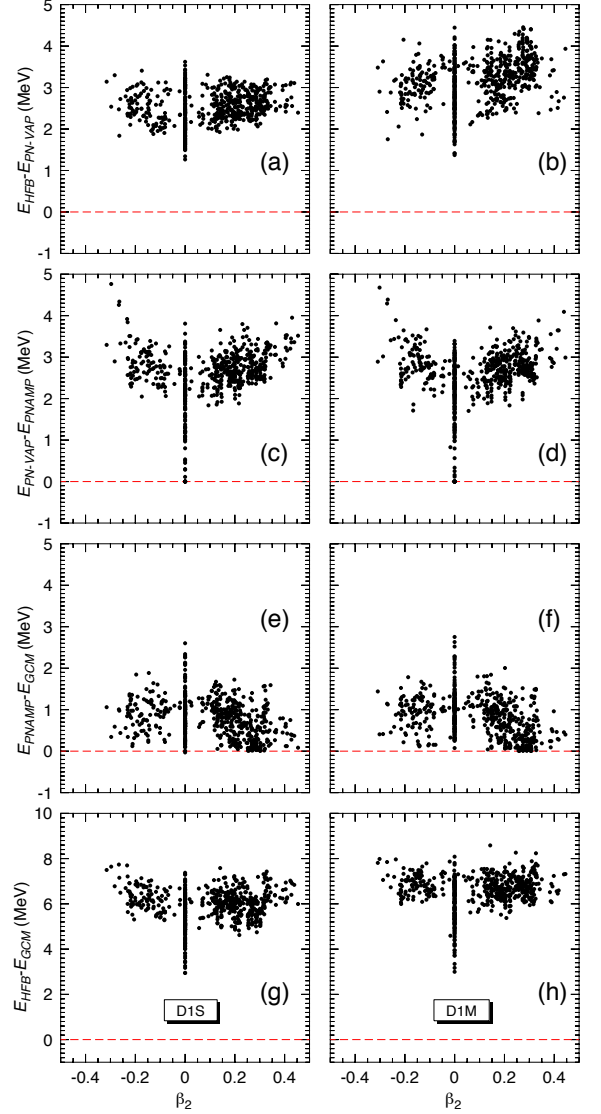


FIG. 4. Same as Fig. 2 but as a function of the quadrupole deformation found at the mean field -HFB- level.

in the PN-VAP and GCM approaches. In the latter, the correlation energy ranges with the D1S (D1M) from 0.0-1.8 (0.0-1.8) MeV, while in the former from 2.0-3.5 (1.8-4.5) MeV approximately. For PNAMP case, a trend of having larger energy gains with increasing $|\beta_2|$ -values is obtained. Similar results are obtained with Skyrme functionals (see Fig. 7 of Ref [18]) showing that these patterns depend on the method rather than the choice of functional.

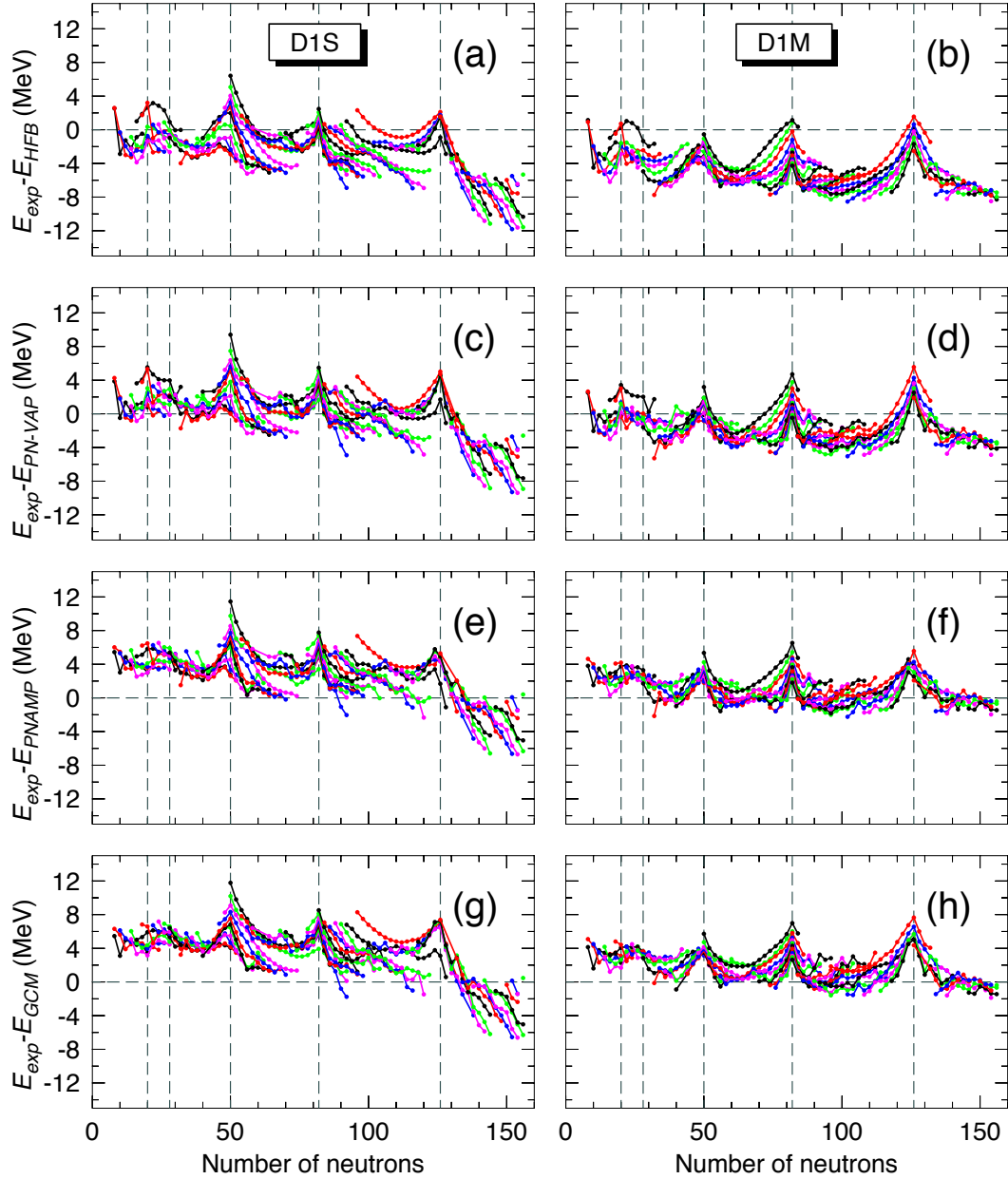


FIG. 5. (color online) Difference between the experimental binding energies (taken from Ref. [29]) and: (a)-(b) HFB; (c)-(d) PN-VAP; (e)-(f) PNAMP; (g)-(h) GCM total energies calculated with the Gogny D1S (left panel) and D1M (right panel) parametrizations. Lines connect isotopic chains starting from $Z = 10$. Black, red, blue, magenta and green lines represent isotopic chains with $Z = x0, x2, x4, x6$ and $x8$, being $x = 1, 2, \dots$, etc. Dashed vertical lines mark the neutron magic numbers 20, 28, 50, 82 and 126.

B. Comparison with experimental data

1. Masses

We now compare the results obtained with the different approximations with the experimental data extracted from the most recent AME [29]. In Fig. 5 the differences between the experimental and theoretical masses

are plotted for the different mean field and beyond mean field approaches. More quantitative results are written in Table I for the D1S and D1M parametrizations.

Starting from the oldest parametrization, i.e., D1S, we notice first its poor performance (compared to the best current HFB mass models [30]) in describing experimental masses. In none of the many-body approaches studied here, the root mean square (RMS) deviation is less than

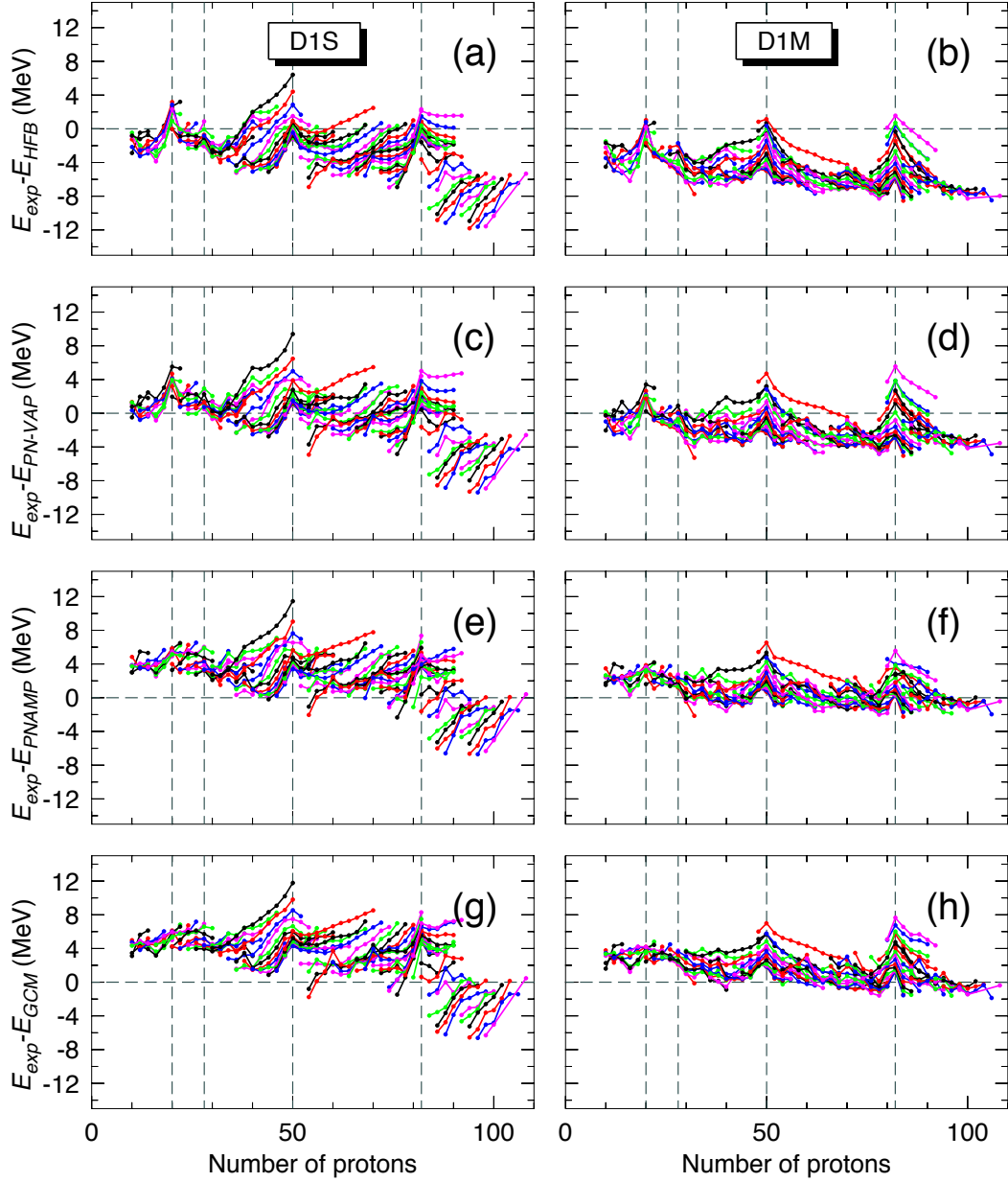


FIG. 6. (color online) Same as Fig. 5 but as a function of the number of protons. Lines connect isotonic chains starting from $N = 10$. Black, red, blue, magenta and green lines represent isotopic chains with $N = x0, x2, x4, x6$ and $x8$, being $x = 1, 2, \dots$, etc. Dashed vertical lines mark the neutron magic numbers 20, 28, 50 and 82.

2.6 MeV. This is explained by three major drawbacks of this parametrization (see left panel of Fig. 5). The first one is the presence of residual shell effects. In all of the approaches, peaks at the neutron magic numbers $N = 50, 82$ and 126 are observed. As it was discussed above, BMF energy gains are smaller in the shell closure nuclei (see Fig. 2(g)). Therefore, these peaks are reduced when BMF effects are taken into account but the reduction is clearly insufficient to bring the theory closer to the experiment. The second drawback is the systematic drift towards less

bound systems in nuclei with increasing neutron excess. The origin of the problem is in the symmetry energy provided by Gogny D1S. This parametrization does not reproduce the correct curvature in the neutron matter equation of state given by *ab-initio* approaches [15] producing a lack of binding energy in neutron rich nuclei. Again, BMF effects do not change this trend. Nevertheless, the spread in light nuclei (from $N = 10-40$) found at the mean field and PN-VAP approximations (Fig. 5(a)) is significantly reduced when PNAMP and GCM are taken

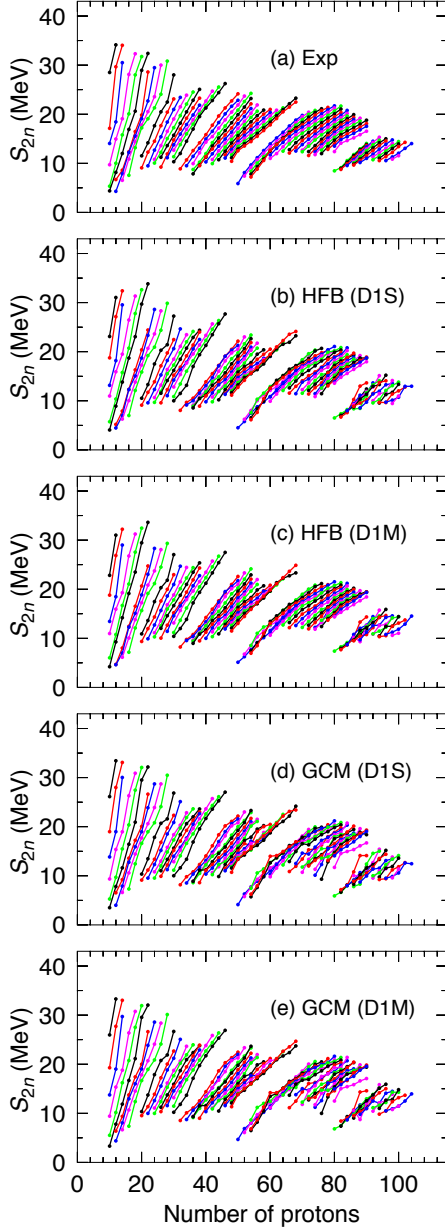


FIG. 7. (color online) Two-neutron separation energies as a function of the number of protons: (a) Experimental data (taken from Ref. [29]); (b) HFB; (d) GCM calculated with the Gogny D1S parametrization and (c) HFB ; (e) GCM calculated with D1M parametrization. Lines connect isotonic chains starting from $N = 10$. Black, red, blue, magenta and green lines represent isotopic chains with $N = x0, x2, x4, x6$ and $x8$, being $x = 1, 2, \dots$, etc.

into account (Figs. 5(e)-(g)). The third drawback is the way in which the parameters of the interaction were obtained. Hence, the parameters of the oldest realizations of the Gogny interaction were fitted to reproduce experimental data with the HFB method but leaving some room for eventual beyond-mean-field effects [31]. How-

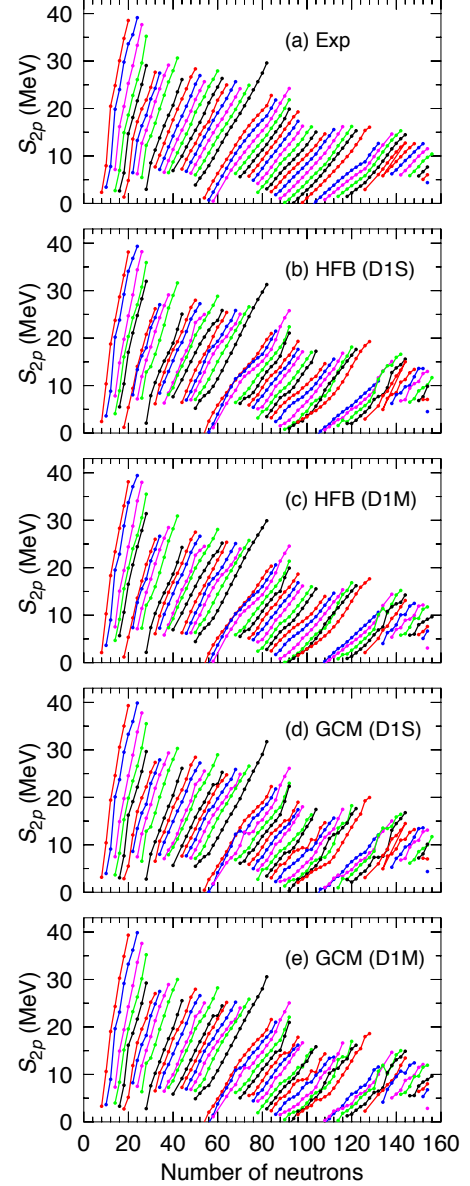


FIG. 8. (color online) Two-proton separation energies as a function of the number of neutrons: (a) Experimental data (taken from Ref. [29]); (b) HFB; (c) GCM calculated with the Gogny D1S parametrization. Lines connect isotopic chains starting from $Z = 12$. Black, red, blue, magenta and green lines represent isotopic chains with $Z = x0, x2, x4, x6$ and $x8$, being $x = 1, 2, \dots$, etc.. The insets show the theoretical S_{2p} versus the experimental ones for the corresponding approach.

ever, some overbinding is still obtained with respect to the experimental values in this region. The evolution of the RMS values given in the second column of Tab. I reflects also this effect, obtaining for the most sophisticated many-body method used in this work a RMS deviation of 4.45 MeV (for 598 masses).

The D1M parametrization [6] was built to correct these shortcomings of the D1S by performing a fit to a large

set of experimental masses using the 5DCH method [20] to include beyond-mean-field effects. That led to a RMS deviation from data of ~ 0.798 MeV (for 2149 masses). Except for the inclusion of triaxiality and the lack of quantum number projections, the 5DCH method can be considered as a gaussian overlap approximation (GOA) of the method used in this work [23]. Let us analyze now the performance of D1M in combination with a method free from such a GOA approximation. In the right panel of Fig. 5 the residuals for the masses obtained with the D1M parametrization are shown. Here we observe that the drift and, partially, the overbinding found with the D1S parametrization are corrected. However, as it was already stated in Ref. [6], strong shell effects are still present and the theoretical results that overestimate the binding energies around the magic neutron numbers, particularly at $N = 50, 82$ and 126 . This behavior is not corrected by including BMF correlations of the kind studied in this work. Nevertheless, the addition of correlations improves the agreement with data with respect to the mean field results. Since the D1M parameters were fitted taking already into account BMF effects, the results at the HFB level are underbound with respect to the experimental values (Fig. 5(b)). A very large RMS deviation is obtained for this approach and a much smaller for the rest (see Table I). However, the correlation energies attained by the GCM are larger than the ones provided by the 5DCH. This produces an excess of total energy also with this parametrization when the full configuration mixing with exact quantum number projection is taking into account (Fig. 5(h)). The final RMS value for the GCM approach with the D1M parametrization is 2.41 MeV (for 598 masses), far from the one reported in Ref. [6].

TABLE I. RMS comparison between theoretical calculations and experimental data for total energies, two neutron and two proton separation energies. All energies are in MeV.

D1S	E	S_{2n}	S_{2p}
HFB	3.53	0.98	1.15
PN-VAP	2.62	1.10	1.11
PNAMP	3.75	0.98	1.00
GCM	4.45	0.95	1.00
D1M	E	S_{2n}	S_{2p}
HFB	5.27	0.90	1.00
PN-VAP	2.50	1.04	0.95
PNAMP	1.79	0.89	0.85
GCM	2.41	0.87	0.88

In order to check the possible shells effects appearing in isotonic chains, we represent in Fig. 6 the residuals obtained for the different many-body approaches and parametrizations as a function of the number of protons. These shell effects, though still present, are slightly less pronounced than in the isotopic chains. This is in agreement with the results found with Skyrme in-

TABLE II. Logarithmic errors and deviations for the 2_1^+ excitation energies computed for GCM-D1S, GCM-D1M, GCM-SLy4 [42] and 5DCH-D1S [20].

	GCM-D1S	GCM-D1M	GCM-SLy4	5DCH-D1S
\bar{R}_E	0.32	0.35	0.51	0.11
σ_E	0.42	0.43	0.38	0.35

teractions [18]. However, it is interesting to note that the relative overbinding found at $Z = 20$ at the HFB level is smoothened out with BMF approaches in both parametrizations while $Z = 50$ and 126 persist. Finally, we observe a clear difference between the results provided by the two parametrizations. For D1M rather symmetric residuals around the shell closures are found while for D1S larger energies are obtained for larger values of Z within a given isotonic chain. Since the isotonic chains start normally with $N > Z$, this behavior reflects again a lack of ground state energy provided by the D1S parametrization in nuclei with neutron excess, i.e., the symmetry energy problem already mentioned.

To conclude this section, we can state that both the symmetry energy problem and the overbinding produced by the inclusion of BMF effects can be solved by modifying the parametrization, as it is almost done with the introduction of the Gogny D1M interaction. However, the energy excess obtained in the magic nuclei (relative to the energy predicted in the mid-shell nuclei), although reduced, is not washed out by taking into account the present BMF effects. It is still an open question whether the current BMF functionals, with parameters self-consistently fitted and probably extended to include other collective degrees of freedom and symmetry restorations, are able to produce flat residuals instead of the parabolic behavior found in Figs. 5-6 (and in Refs. [6, 15, 18, 20]). These tasks are highly demanding, both the refit of the interaction and the inclusion of, for example, pairing fluctuations [35], triaxial [26, 36, 37] and/or octupole [38, 39] shapes with the corresponding symmetry restorations and configuration mixing. On the other hand, it is possible that the central, spin-orbit and density-dependent terms of the starting Gogny interaction have to be modified including, for instance, explicit tensor terms [40].

2. Two particle separation energies

Most of the times, the relevant quantities for calculating reaction rates, Q -values, etc., with astrophysical interest are not the absolute energies shown in the previous section but energy differences between those masses. We analyze now its performance on two-nucleon separation energies (S_{2n}, S_{2p}), since the present GCM method with the Gogny functional is not well developed for computing odd-nuclei yet:

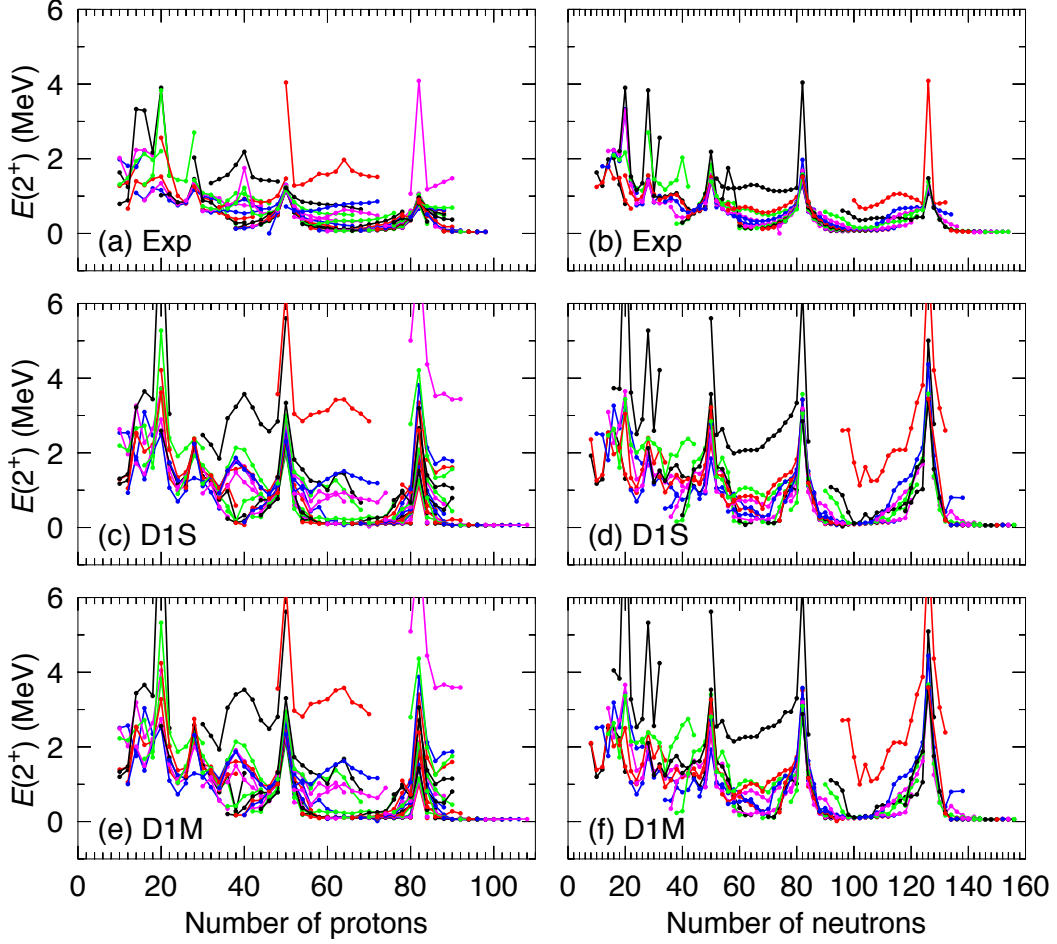


FIG. 9. (color online) 2^+_1 excitation energies for: (a)-(b) Experimental data (taken from Ref. [41]); (c)-(d) GCM-Gogny D1S; and (e)-(f) GCM-Gogny D1M. Lines connect isotonic chains starting from $N = 10$ (left panel) and isotopic chains starting from $Z = 10$ (right panels). The color code is the same as in previous figures.

$$\begin{aligned} S_{2n}(Z, N) &= E(Z, N-2) - E(Z, N) \\ S_{2p}(Z, N) &= E(Z-2, N) - E(Z, N) \end{aligned} \quad (14)$$

These quantities are plotted in Figs. 7- 8 and analyzed quantitatively in Table I. The overall behavior of the experimental values is quite well reproduced. The RMS deviations from experimental values for S_{2n} and S_{2p} are much better than in the masses for both parametrizations. However, we observe important local differences between the experimental data and theory. On the one hand, the experimental curves are much smoother, having always for a constant number of protons (neutrons) a continuous decrease in the S_{2n} (S_{2p}) when adding neutrons (protons). This is not the case for the theoretical data, where jumps and crossings between isotonic (isotopic) chains in the S_{2n} (S_{2p}) separation energies are shown. This drawback is obtained all over the nuclear

chart independently on the parametrization and is a bit larger in the GCM approach than in the HFB result. Finally, neutron and proton shell gaps associated to magic numbers are predicted to be larger than the experimental values. Correlations beyond the static mean field tend to reduce these gaps more efficiently in $N = 20, 28$ and $Z = 20, 28, 50$ but the reduction is not enough to reproduce the actual gaps in $N = 50, 82, 126$ nor $Z = 82$. The shell quenching obtained by including BMF effects reported by Bender et al. in Ref. [19] and by Delaroche et al. in Ref. [20] is only partially reproduced here. In addition, the latter results are much smoother than the results shown in Figs. 7-8 probably due to the GOA approximations used in those references.

3. 2_1^+ excitation energies

We finally compare the 2_1^+ excitation energies obtained with our present GCM global calculations with the experimental data compiled in Ref. [41]. It is important to note that in this case the convergence of the results are not fully guaranteed, especially in heavy nuclei where a working basis including eleven major oscillator shells is definitely too small. Therefore, the values obtained with this reduced space must be taken with caution. In any case, we consider these results relevant to extract a global performance of the method, and, in particular, to compare the results provided by the two Gogny parametrizations for this observable. We can also compare with the results of similar studies already reported with the Skyrme SLy4 [42] (with a topological gaussian overlap approximation in the angular momentum projection and a limited number of intrinsic states in the GCM) and Gogny D1S [20] within the 5DCH framework.

Both the experimental values and the results of the GCM calculations for the 2_1^+ energies are shown in Fig. 9. We observe clearly an enhancement of the excitation energies at the proton and neutron magic numbers. Additionally, the 2_1^+ excitation energies corresponding to $N = 20, 28, 50, 82$ and 126 isotonic chains and Ca, Ni, Sn and Pb isotopes are clearly above the rest both experimentally and in the calculations. On the other hand, we see that the two parametrizations provide almost identical results for this observable even though they behave very different for masses. The global behavior of the experimental data is well reproduced although the calculations show a less smooth behavior and a systematic overestimation of the experimental values.

The latter drawback can be better seen in Fig. 10(a)-(b), where the theoretical values versus the experimental energies are represented for D1S and D1M parametrizations respectively. Although we observe a clear correlation between the two quantities, the theoretical predictions tend to overestimate the empirical values. We do not find significant differences between the D1S and D1M parametrizations. To better estimate quantitatively the differences with the experimental results we follow the analysis performed in Refs. [42]-[20]. There, the so-called logarithmic error $-R_E$ - and its standard deviation $-\sigma_E$ - from the average $-\bar{R}_E$ - are defined as:

$$R_E = \log [E(2_1^+)_{\text{th}}/E(2_1^+)_{\text{exp}}] \quad (15)$$

$$\sigma_E = \langle (R_E - \bar{R}_E)^2 \rangle^{1/2} \quad (16)$$

In Fig. 10(c)-(d) we show histograms representing the number of nuclei with a given value of R_E for D1S and D1M parametrizations. We find rather symmetric distributions with mean values and standard deviations of $\bar{R}_E = 0.32(0.35)$ and $\sigma_E = 0.42(0.43)$ respectively for D1S (D1M). Similar results are obtained with Skyrme SLy4 [42] (see Table II). This systematic drift towards larger values is a consequence of the variational method.

In this framework, the ground state 0_1^+ are favored with respect to other states, pulling down its energy and stretching the final spectra. The inclusion of additional degrees of freedom such as triaxiality, time-reversal symmetry breaking and quasiparticle excitations, which are more relevant in the excited states than in the ground state, allows a variational description of these excited states and the excitation energies can be reduced. For example, local studies with a GCM method including triaxial angular momentum projection [26, 36, 37] or pairing fluctuations [35] have already shown this effect. On the other hand, quantum number projections and GCM can modify significantly both the equilibrium deformation of the system (^{32}Mg is the paradigm for this effect [25]) and the collective masses. Since these parametrizations are not fitted with using the BMF many-body states of this work, the MF and BMF collective behavior can be different. For instance, angular momentum projection could overestimate a quadrupole deformation that could be correct at the HFB level. Therefore, the excitation energies should be taken into account in a future refit of the interaction.

We finally comment on the smaller deviation and dispersion obtained with Gogny D1S using the 5DCH method [20] shown in Table II. In this case, the inclusion of the triaxial degree of freedom and the fit of the inertia parameters with a cranking approximation can improve the description of the 2_1^+ excitation energies. However, since 5DCH does not include either particle number or angular momentum projection, spurious contributions of MF states with the wrong quantum numbers can produce a collapse of the excited states [35]. In any case, further analyses, beyond the scope of this work, are needed to compare the 5DCH approach with a full SCCM approximation.

IV. SUMMARY AND OUTLOOK

In this work, correlation energies, total energies, two neutron separation energies and 2_1^+ excitation energies for a large set of nuclei along the nuclear chart have been presented. The theoretical results have been obtained by using self-consistent mean field (HFB) and beyond-mean-field (BMF) methods, including exact particle number and angular momentum restorations and exact axial quadrupole shape mixing. The underlying interaction used in all of the calculations was Gogny with two different parametrizations, D1S and D1M. Both parametrizations give similar correlation energies with respect to their mean field solutions, except for the particle number projection (PN-VAP) where a rather flat behavior is found for D1S while for D1M an increase with larger particle numbers is obtained.

Compared to the experimental data, the D1S parametrization shows a symmetry energy problem which produces a lack of binding energy in neutron rich systems. This fact is reflected in a drift in the difference

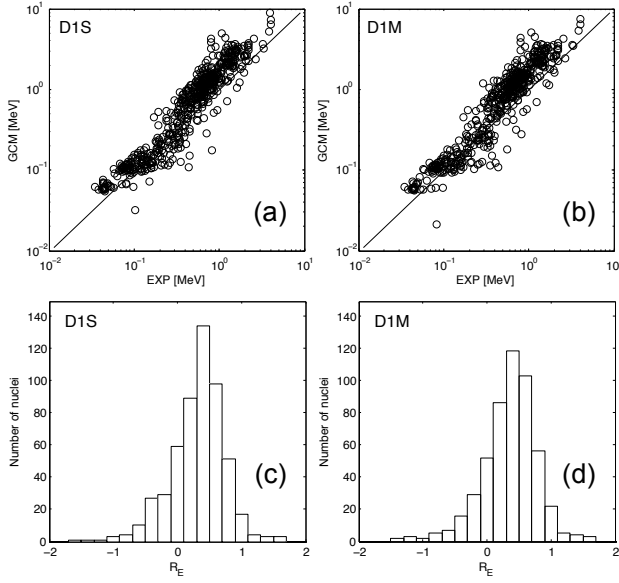


FIG. 10. GCM versus experimental 2_1^+ excitation energies for (a) D1S and (b) D1M parametrizations. Histograms of the logarithmic errors of the 2_1^+ states.

between theoretical and experimental energies for nuclei with a neutron excess which is corrected in the D1M parametrization. However, strong shell effects (stronger as a function of the neutron number) are still present in both realizations and parabolic instead of flat residuals are found between two consecutive magic numbers. BFM correlations tend to reduce these differences since rotational and vibrational corrections are larger in the mid-shell than in closed shell nuclei, but this reduction is not sufficient to remove the difference between the experimental and theoretical values.

Energy differences such as two-neutron separation energies are in a better agreement with experimental data but still not satisfactory. Some problems like artificial jumps, crossing and overestimation of the shell gaps are found in the calculations and they are not corrected by including BMF effects.

Additionally, we have reported the results for 2_1^+ excitation energies calculated with $N_{s.h.o.} = 11$ shells. We have obtained similar results for D1S and D1M parametrizations, having a systematic stretching of the 2_1^+ energies which is more related to the method used to solve the many-body problem rather than the parametrization itself.

As an outlook, some improvements should be taken into account in the near future, in particular:

1. Convergence of the results with the properties of the harmonic oscillator working basis.
2. Triaxial and other degrees of freedom should be included explicitly in the calculations.
3. A new parametrization of the Gogny interaction (or any other type of energy density functional) including the SCCM corrections in the fitting procedure is desirable.

Finally, new experimental data would be very helpful to constrain further the current and future models.

ACKNOWLEDGEMENTS

This work was supported by the BMBF-Verbundforschungsprojekt number 06DA7047I, the Ministerio de Economía y Competitividad-Programa Ramón y Cajal 2012 number 11420 and the Helmholtz Association through the Nuclear Astrophysics Virtual Institute (VH-VI-417).

-
- | | |
|--|---|
| <p>[1] K. Blaum, Phys. Repts. 425, 1 (2006).
 [2] P. Möller, J. R. Nix, W. D. Myers, and W. J. Swiatecki, At. Data Nucl. Data Tables 59, 185 (1995).
 [3] N. Wang, M. Liu, and X. Wu, Phys. Rev. C 81, 044322 (2010).
 [4] J. Duflo and A. P. Zuker, Phys. Rev. C 52, R23 (1995).
 [5] S. Goriely, N. Chamel, and J. M. Pearson, Phys. Rev. C 88, 024308 (2013).
 [6] S. Goriely, S. Hilaire, M. Girod, and S. Péru, Phys. Rev. Lett. 102, 242501 (2009).
 [7] A. Arcones and G. Martínez-Pinedo, Phys. Rev. C 83, 045809 (2011).
 [8] S. Brett, I. Bentley, N. Paul, R. Surman, and A. Aprahamian, Eur. Phys. J. A 48, 184 (2012).
 [9] R. Roth, J. Langhammer, A. Calci, S. Binder, and P. Navratil, Phys. Rev. Lett. 107, 072501 (2011).
 [10] D. J. Dean and M. Hjorth-Jensen, Phys. Rev. C 69, 054320 (2004).</p> | <p>[11] H. Hergert, S. Binder, A. Calci, J. Langhammer, and R. Roth, Phys. Rev. Lett. 110, 242501 (2013).
 [12] V. Soma, C. Barbieri, and T. Duguet, Phys. Rev. C 87, 011303 (2013).
 [13] J. D. Holt, J. Menéndez, and A. Schwenk, Phys. Rev. Lett. 110, 022502 (2013).
 [14] N. Chamel, S. Goriely, and J.M. Pearson, Nucl. Phys. A 812, 72 (2008).
 [15] F. Chappert, M. Girod, and S. Hilaire, Phys. Lett. B 668, 420 (2008).
 [16] S. Goriely, M. Samyn, and J. M. Pearson, Phys. Rev. C 75, 064312 (2007).
 [17] M. Bender, P.-H. Heenen, and P.-G. Reinhard, Rev. Mod. Phys. 75, 121 (2003).
 [18] M. Bender, G. F. Bertsch, and P.-H. Heenen, Phys. Rev. C 73, 034322 (2006).
 [19] M. Bender, G. F. Bertsch, and P.-H. Heenen, Phys. Rev. C 78, 054312 (2008).</p> |
|--|---|

- [20] J.-P. Delaroche, M. Girod, J. Libert, H. Goutte, S. Hilaire, S. Péru, N. Pillet, and G. F. Bertsch, Phys. Rev. C 81, 014303 (2010).
- [21] J.-F. Berger, M. Girod, and D. Gogny, Nucl. Phys. A428, 23c (1984).
- [22] J.-F. Berger, M. Girod, and D. Gogny, Comput. Phys. Commun. 63, 365 (1991).
- [23] P. Ring, and P. Schuck, *The nuclear many-body problem*, Springer-Verlag, Berlin, 1980.
- [24] D. Lacroix, T. Duguet, and M. Bender, Phys. Rev. C 79, 044318 (2009).
- [25] R. Rodríguez-Guzmán, J. L. Egido, and L. M. Robledo, Nucl. Phys. A 709, 201 (2002).
- [26] T. R. Rodríguez, J. L. Egido, Phys. Rev. C 81, 064323 (2010).
- [27] T. R. Rodríguez, J. L. Egido, Phys. Rev. Lett. 99, 062501 (2007).
- [28] M. Anguiano, J. L. Egido, and L. M. Robledo, Nucl. Phys. A696, 467 (2001).
- [29] M. Wang, G. Audi, A.H. Wapstra, F.G. Kondev, M. MacCormick, X. Xu, and B. Pfeiffer, Chinese Phys. C 36, 1603 (2012).
- [30] S. Goriely, N. Chamel, and J. M. Pearson, Phys. Rev. C 88, 061302(R) (2013).
- [31] J. Dechargé and D. Gogny, Phys. Rev. C 21, 1568 (1980).
- [32] L. M. Robledo, HFBAXIAL code, Universidad Autónoma de Madrid (2002).
- [33] <https://wiki.gsi.de/cgi-bin/view/Linux/GridEngine>
- [34] <http://csc.uni-frankfurt.de/index.php?id=51&L=0>
- [35] N. L. Vaquero, J. L. Egido, and T. R. Rodríguez, Phys. Rev. C 88, 064311 (2013).
- [36] M. Bender and P.-H. Heenen, Phys. Rev. C 78, 024309 (2008).
- [37] J. M. Yao, J. Meng, P. Ring, and D. Vretenar, Phys. Rev. C 81, 044311 (2010).
- [38] P. A. Butler and W. Nazarewicz, Rev. Mod. Phys. 68, 349 (1996).
- [39] E. Garrote, J. L. Egido, and L. M. Robledo, Phys. Rev. Lett. 80, 4398 (1998).
- [40] T. Otsuka, T. Matsuo, and D. Abe, Phys. Rev. Lett. 97, 162501 (2006).
- [41] S. Raman, C. W. Nestor, and P. Tikkanen, At. Data Nucl. Data Tables 78, 1 (2001).
- [42] B. Sabbey, M. Bender, G. F. Bertsch, and P.-H. Heenen, Phys. Rev. C 75, 044305 (2007).